Volume 26
Number 8
21 April 2026
Pages 2385–2624

Lab on a Chip

Devices and applications at the micro- and nanoscale

rsc.li/loc

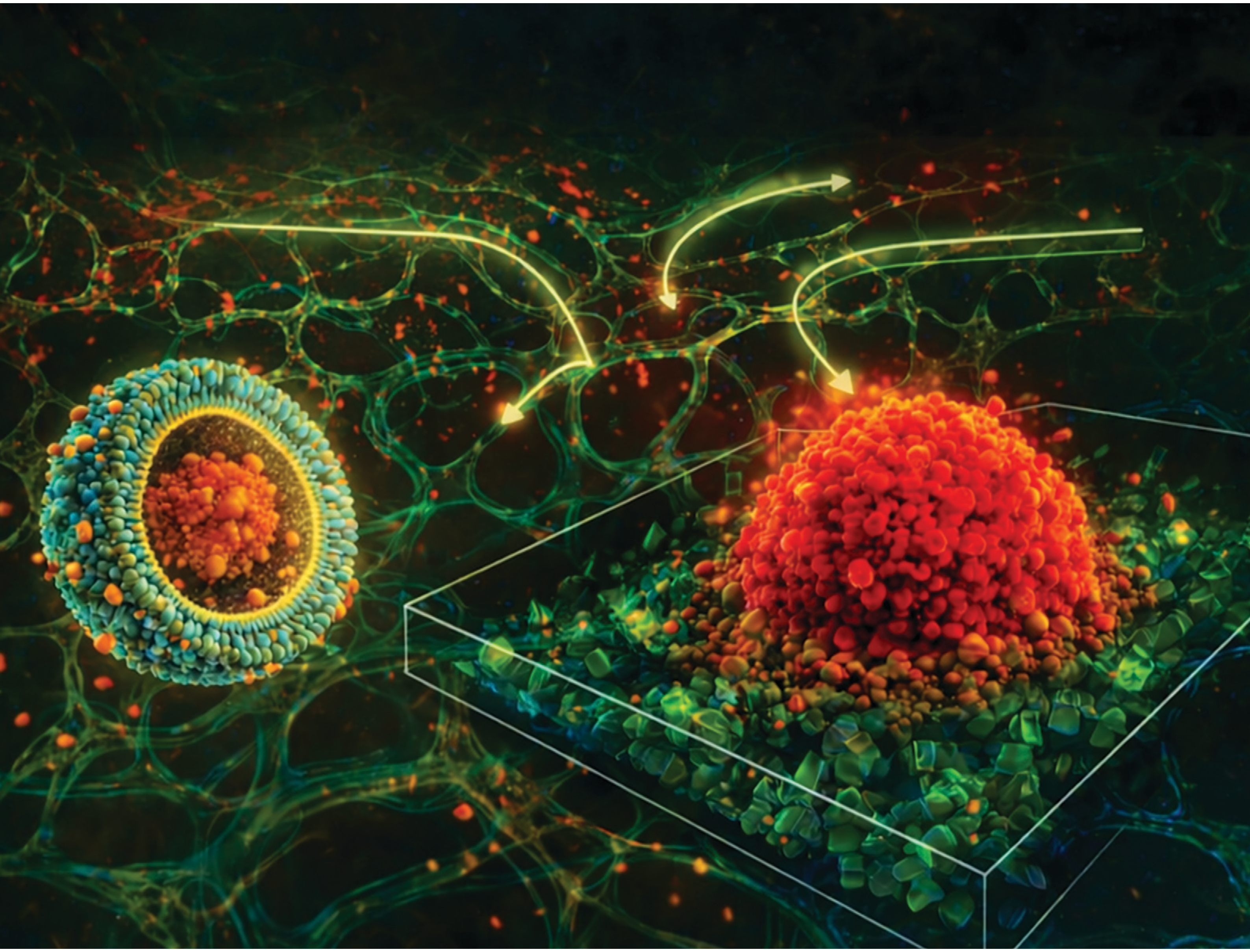

ISSN 1473-0197

ROYAL SOCIETY
OF **CHEMISTRY**

PAPER
Jung Y. Han, Jihoon Ko *et al.*
A tumor spheroid array chip for high-fidelity evaluation of
liposomal drug delivery through the EPR effect

Lab on a Chip

PAPER

View Article Online
View Journal | View Issue

Cite this: *Lab Chip*, 2026, **26**, 2439

A tumor spheroid array chip for high-fidelity evaluation of liposomal drug delivery through the EPR effect

Yedam Lee,† Sujin Kim,† Hyeyeon Koh, Yeonwoo Park,
Jung Y. Han* and Jihoon Ko *

Received 18th September 2025,
Accepted 5th December 2025

DOI: 10.1039/d5lc00893j

rsc.li/loc

Conventional two-dimensional (2D) culture systems fail to recapitulate the structural and functional complexity of the tumor microenvironment (TME), limiting their utility for preclinical drug evaluation. Here, we present a perfusable, high-throughput microfluidic Tumor Spheroid Array (TSA)-Chip that supports dynamic co-culture of tumor spheroids and vascular networks under perfusable conditions. The platform enables real-time visualization and quantitative analysis of nanoparticle transport, therapeutic response, and vascular remodeling. Fluorescent liposome tracking revealed EPR-like, tumor-selective accumulation, which was absent in 2D or tumor-free models. Liposomal 5-fluorouracil (5-FU) induced localized cytotoxicity and peritumoral vessel pruning while preserving overall vascular integrity. Furthermore, combination treatment with Cyramza™ (ramucirumab) enhanced tumor suppression and barrier normalization. Compared to conventional models, the TSA-chip offers robust analytical capabilities for assessing nanocarrier delivery and combination therapy effects in a scalable and physiologically relevant format, advancing its utility in precision oncology research.

1. Introductions

Despite significant progress in cancer research, conventional two-dimensional (2D) cell culture models remain inadequate for replicating the complex cellular and biochemical dynamics of the tumor microenvironment (TME).[1,2] These systems fail to capture critical processes such as vascular transport, tumor angiogenesis, and dynamic vascular permeability, all of which are critical for understanding cancer progression and evaluating therapeutic efficacy. Consequently, drug screening in 2D systems often overestimates treatment responses and provides limited predictive value for clinical outcomes.[3]

Three-dimensional (3D) culture models offer improved physiological relevance;[4] however, many still lack essential components such as perfusable vasculature, biomechanical stimulation, or spatial tissue organization required to emulate *in vivo* conditions.[5,6] Organ-on-a-chip (OoC) technologies address these limitations by integrating 3D cultures into microfluidic platforms that enable controlled fluid flow, tunable microenvironments, and real-time imaging.[7–9] These platforms support the self-assembly of vascular networks and the maintenance of physiologically relevant gradients of oxygen and nutrients.[10–12] In cancer research, OoC-based models have successfully recapitulated key TME features such as hypoxia, angiogenesis, stromal interaction, and extracellular matrix (ECM) stiffness, providing robust platforms for mechanistic studies and therapeutic evaluation.[13–16]

With the rise of advanced drug delivery strategies, particularly nanocarrier-based chemotherapeutics, there is a growing need for physiologically faithful *in vitro* models to assess nanoparticle transport and efficacy.[17,18] Liposomal formulations, such as liposome-encapsulated 5-fluorouracil (5-FU), have demonstrated improved pharmacokinetics, reduced systemic toxicity, and enhanced tumor-specific accumulation *via* the enhanced permeability and retention (EPR) effect.[19–21] However, the therapeutic performance of liposomal drugs critically depends on the vascular architecture, permeability, and interstitial transport properties of the tumor tissue.[22,23] Conventional static models lacking perfusable vasculature fail to replicate these transport phenomena and are thus insufficient for predicting nanoparticle accumulation, vascular toxicity, and clearance.[24,25]

In this study, we introduce a perfusable TME model integrated into a high-throughput microfluidic OoC platform, termed the Tumor Spheroid Array Chip (TSA-Chip). Multicellular tumor spheroids, composed of colorectal cancer (CRC) cells, vascular endothelial cells, and fibroblasts, were

---

Department of BioNano Technology, Gachon University, Seongnam-si, Gyeonggi-do 13120, Republic of Korea. E-mail: jhan@gachon.ac.kr, koch@gachon.ac.kr

† These authors contributed equally to this work.

embedded within a fibrin-based hydrogel to promote self-assembled vascularization, enable continuous media perfusion, and allow real-time imaging.[26] This platform supports quantitative assessment of vascular permeability and intratumoral drug distribution under physiologically relevant flow conditions. To demonstrate its utility, we evaluated the delivery efficiency and therapeutic outcomes of both liposomal and free 5-FU formulations. We hypothesized that liposomal encapsulation would enhance tumor accumulation and reduce vascular leakage *via* the EPR effect.[27–29] Our findings highlight the importance of nanocarrier-based drug delivery strategies and underscore the potential of perfusable TME models to improve preclinical predictability and accelerate the development of precision oncology therapies.[30–32]

2. Materials and methods

2.1. Preparation of 5-FU-liposomes

5-FU-loaded liposomes (5-FU-Lip) were prepared using the thin-film hydration method, followed by ultrasonication and membrane extrusion, as previously described.[33] Briefly, 1,2-dimyristoyl-*sn*-glycero-3-phosphocholine (DMPC) and cholesterol were dissolved in chloroform and mixed at a total lipid concentration of 20 mM in a 60 : 40 molar ratio. The lipid mixture was transferred into a scintillation vial, and the solvent was evaporated under a gentle stream of nitrogen to form a thin lipid film along the inner wall. To ensure complete solvent removal, the film was further dried under vacuum overnight. The dried lipid film was hydrated with phosphate-buffered saline (PBS, pH 7.4) containing 1 mM 5-FU at 70 °C for 40 minutes, with intermittent gentle mixing. The resulting multilamellar vesicles were subjected to probe sonication at 100 W for 15 minutes in an ice bath and subsequently extruded 10 times through a 0.22 μm polycarbonate membrane filter (Whatman, USA) to yield uniformly sized unilamellar vesicles. To remove unencapsulated 5-FU, the liposome suspension was transferred to dialysis tubing (MWCO 10 kDa; ThermoFisher Scientific, USA) and dialyzed against an ~60-fold excess volume of PBS for 2 hours at room temperature. The final liposomal formulation was stored at 4 °C until use. The encapsulated drug concentration was quantified by UV-visible spectroscopy (Jasco V-770, Japan) by comparing the absorbance value before and after dialysis.

2.2. TSA-Chip design and fabrication

The TSA-Chip was fabricated *via* injection molding in polystyrene (PS), based on our previously developed microfluidic high-throughput 3D cell culture.[34] The chip geometry and array layout were designed using computer-aided design (CAD) software to ensure compatibility with standard optical imaging and high-content screening workflows. Aluminum alloy molds (Al 7075) were precision-machined and polished to create smooth channel surfaces for reliable fluid handling. Injection molding was carried out under the following conditions: a clamping force of 130 tons, a maximum injection pressure of 68 bar, a cycle time of 30 seconds, and a nozzle temperature of 230 °C. To define the open microchannel architecture, a pressure-sensitive adhesive (PSA) film (IS08820, IS Solution) was pre-applied to the bottom surface of each chip. To improve surface wettability and support consistent hydrogel patterning, the chips were treated with air plasma (PS-100, PLASOL, Korea) at 75 W for 3 minutes prior to use. This streamlined manufacturing process enabled scalable production of TSA-Chips with high reproducibility, structural uniformity, and compatibility with automated analysis.

2.3. Cell preparation

To establish a perfusable TME, three human cell types were used: human umbilical vein endothelial cells (HUVECs), human lung fibroblasts (LFs), and CRC cells (HCT-116). HUVECs and LFs were purchased from Lonza (Basel, Switzerland) and cultured according to the manufacturer's protocols in Endothelial Growth Medium-2 (EGM-2) and Fibroblast Growth Medium-2 (FGM-2), respectively. HUVECs were used at passages 4–6, and LFs at passages 6–8. HCT-116 cells (colorectal carcinoma, ATCC® CCL-247™) were maintained in Dulbecco's modified Eagle medium (DMEM; Gibco) supplemented with 10% fetal bovine serum (FBS; Gibco) and 100 U mL^{-1} penicillin–streptomycin (Gibco). All cells were incubated at 37 °C in a humidified atmosphere containing 5% CO$_2$ and were subcultured every 2–3 days. Cells were recollected for use in OoC upon reaching 80–90% confluency to ensure optimal viability and performance.

2.4. Multicellular tumor spheroid formation

Multicellular tumor spheroids were generated using HCT-116 CRC cells, LFs, and HUVECs. HCT-116 cells were resuspended in StemFIT 3D hydrogel medium (Fitton, Korea), which promotes uniform spheroid formation under non-adherent conditions. A total of 0.9×10^6 HCT-116 cells in 1 mL suspension were seeded into each well of a low-attachment plate and incubated at 37 °C with 5% CO$_2$ for 24 hours. Following initial spheroid formation, the medium was gently removed and replaced with a suspension of LFs (0.3×10^6 cells per well). The plate was incubated for an additional 24 hours to allow stromal cells to incorporate around the tumor spheroids. Subsequently, HUVECs were added at a total density of 1.0×10^6 cells, corresponding to 0.3×10^6 cells per well, and co-cultured for another 24 hours to establish vascular association. The resulting multicellular tumor spheroids consisted of cancer cells, fibroblasts, and endothelial cells organized in a layered architecture. Spheroids were gently harvested and transferred into the pre-conditioned microfluidic chips for subsequent experiments.

2.5. Reconstruction of the 3D perfusable TME

To reconstruct a perfusable TME, multicellular tumor spheroids were embedded within the central channel of the TSA-Chip along with HUVECs, LFs, and a fibrin-based hydrogel. The hydrogel was prepared by mixing fibrinogen (12 mg mL^{-1}; Sigma-Aldrich) with aprotinin (0.15 U mL^{-1}; Sigma-Aldrich) at a volume ratio of 250 : 40, yielding a final fibrinogen concentration of 3.0 mg mL^{-1}. A total volume of 7.5 μL of this hydrogel mixture containing HUVECs (6×10^6 cells per mL), LFs (2×10^6 cells per mL), and pre-formed multicellular spheroids was introduced into the central channel. Thrombin (1 U mL^{-1}; Sigma-Aldrich) was added immediately before loading to initiate fibrin polymerization. On day 2 of culture, 30 μL of HUVEC suspension was injected into each side channel through designated inlets to promote endothelial lining along the hydrogel interface. To establish hydrostatic flow, a culture medium was added to the reservoirs, and a physiologically relevant interstitial flow was generated by adjusting the relative height difference between inlet and outlet wells.

2.6. Bead assay for perfusability

The perfusability of the 3D TME model was evaluated on day 6 using a fluorescent microbead assay. Fluorescent polystyrene microbeads (2.0 μm diameter) were suspended in cell culture medium and introduced into the inlet reservoir of the TSA-Chip. Real-time tracking of bead movement through the vascular network was performed using confocal laser scanning microscopy. Beads were observed migrating from the inlet toward the central tumor region, following vessel-like paths formed within the hydrogel. *Z*-Stack fluorescence imaging confirmed that microbeads localized within the luminal space of the vascular structures, indicating the presence of open and interconnected channels.

2.7. Permeability assay

To evaluate endothelial barrier integrity and vascular permeability, a fluorescence-based assay was performed using fluorescein isothiocyanate (FITC)-conjugated dextran (20 kDa; Sigma Aldrich). Prior to tracer introduction, all medium reservoirs were carefully aspirated to remove residual fluid and establish consistent flow conditions. A total of 50 μL of FITC-dextran solution was introduced into the inlet reservoir adjacent to the hydrogel region to generate directional flow across the endothelial interface. Time-lapse fluorescence imaging was conducted using a confocal microscope (Eclipse Ti2; Nikon, Japan) under incubated conditions to maintain cellular viability and junctional stability. Images were acquired every 15 seconds over a 3-minute interval, focusing on both the vascularized hydrogel region and the adjoining cellular boundaries. Fluorescence intensity was quantified using ImageJ software (NIH, USA). The permeability coefficient was calculated based on the rate of FITC-dextran diffusion across the endothelium, following a previously described method.[35]

2.8. Drug treatment

The therapeutic response of the perfusable TME model was assessed following treatment with 5-FU-Lip (100 μM) and ramucirumab (Cyramza™; 10 μM). Drug administration was initiated on day 4 of on-chip culture and maintained for 24 hours. For the monoclonal antibody group, ramucirumab was diluted in EGM-2 to a final concentration of 10 μM and added to the media reservoirs. For the chemotherapeutic group, 5-FU-Lip was also prepared in EGM-2 at 100 μM and introduced *via* the same method. All devices were maintained under standard culture conditions (37 °C, 5% CO_2) throughout the treatment period.

2.9. Immunostaining

For immunofluorescence analysis, cells within the TSA-Chip were fixed with 4% (w/v) paraformaldehyde in PBS for 15 minutes at room temperature. Following fixation, samples were permeabilized with 0.2% (v/v) Triton X-100 in PBS for 20 minutes to allow antibody penetration. To minimize nonspecific binding, blocking was performed using 1% bovine serum albumin in PBS for 1 hour at room temperature. Primary staining was conducted using Alexa Fluor 594-conjugated anti-CD31 antibody (1 : 200 dilution), Alexa Fluor 594-conjugated anti-CD326 (EpCAM) antibody (1 : 200 dilution), and DAPI (1 : 1000 dilution) for nuclear visualization. All staining solutions were prepared in blocking buffer. Confocal fluorescence imaging was carried out using a spinning disk confocal microscope (CQ1, Yokogawa) to acquire high-resolution *z*-stack images, enabling visualization of vascular networks and tumor spheroids within the microfluidic device.

2.10. Quantitative image analysis

Confocal microscopy images were analyzed using ImageJ and custom image processing pipelines to quantify spheroid morphology and viability. *Z*-Stack images were projected along the *Z*-axis using the maximum intensity projection method to generate 2D representations for analysis. Due to variability in spheroid morphology and contrast, pre-processing steps were applied to improve segmentation accuracy. These included histogram equalization and signal normalization, implemented using Python (version 3.7) and the OpenCV image processing library. Spheroid contours were extracted from the processed images to define regions of interest. Within each identified region, green fluorescence intensity corresponding to EpCAM staining was quantified to determine the total spheroid area. Red fluorescence from propidium iodide staining was used to identify non-viable regions. These measurements were used to calculate spheroid size and relative viability for each condition. All quantified data were analyzed using GraphPad Prism (version 9). The spheroid area and viability were statistically compared across treatment groups to assess drug efficacy under different experimental conditions.

2.11. Statistical analysis

All quantitative data were analyzed and visualized using GraphPad Prism (GraphPad Software, USA). Results are presented as mean values with standard error of the mean. Statistical comparisons between groups were performed using unpaired two-tailed *t*-tests. Significance levels were denoted as follows: $*p < 0.05$, $**p < 0.01$, $***p < 0.001$, $****p < 0.0001$. Differences without statistical significance were indicated as not significant (ns). The value "*n*" means the number of individual chips used for each experimental group, with each chip containing one independently cultured tumor spheroid and its associated vascular network.

3. Results

3.1. Development of the TSA-Chip for functional modeling of liposomal drug delivery

To enable physiologically relevant drug evaluation in a perfusable TME, we developed the TSA-Chip—a microfluidic platform that integrates tumor spheroids with self-assembled vasculature in a high-throughput format. As shown in Fig. 1A, the TSA-Chip comprises eight independent microfluidic units, each featuring a central gel region flanked by two media channels. The design allows for a sequential loading process: (1) multicellular tumor spheroids co-embedded with HUVECs and LFs in a fibrin gel; and (2 and 3) EC suspensions injected into both side channels to form endothelialized interfaces with the hydrogel. This configuration enables angiogenic sprouting from EC-lined channels into the fibrin matrix, allowing continuous perfusion and direct media exchange throughout the culture period. Following gel polymerization, tumor spheroids are spatially confined within the central matrix, while the adjacent ECs self-organize into lumenized microvessels. The open-channel architecture facilitates spatiotemporal control of hydrostatic flow and enables direct administration of therapeutic agents through the media reservoirs, thereby mimicking systemic drug delivery routes observed *in vivo*.

The conceptual design for functional drug transport is illustrated in Fig. 1B. Liposomes introduced through the endothelialized channels are designed to travel along the lumenized microvessels and access vascular gaps near the tumor region in a manner consistent with the EPR effect. After reaching this region, the released 5-FU is expected to induce localized cytotoxic stress and reduce angiogenic activity. This schematic outlines the functional principles that the TSA-Chip is built to support and provides a conceptual link between the platform structure described above and the therapeutic analyses presented in later sections.

3.2. Perfusable vascular networks enable physiological transport in the TSA-Chip

To establish a functional and perfusable TME, we optimized microvascular network formation within the TSA-Chip by embedding tumor spheroids, HUVECs and LFs. HUVECs were additionally seeded into the adjacent media channels to promote endothelial lining along the gel interface, which promoted the development of interconnected, lumenized microvessels capable of physiological transport. To determine optimal stromal conditions, LF density was systematically varied from 1.0 to 6.0 × 10^6 cells per mL while maintaining the HUVEC density at 6.0 × 10^6 cells per mL. As shown in

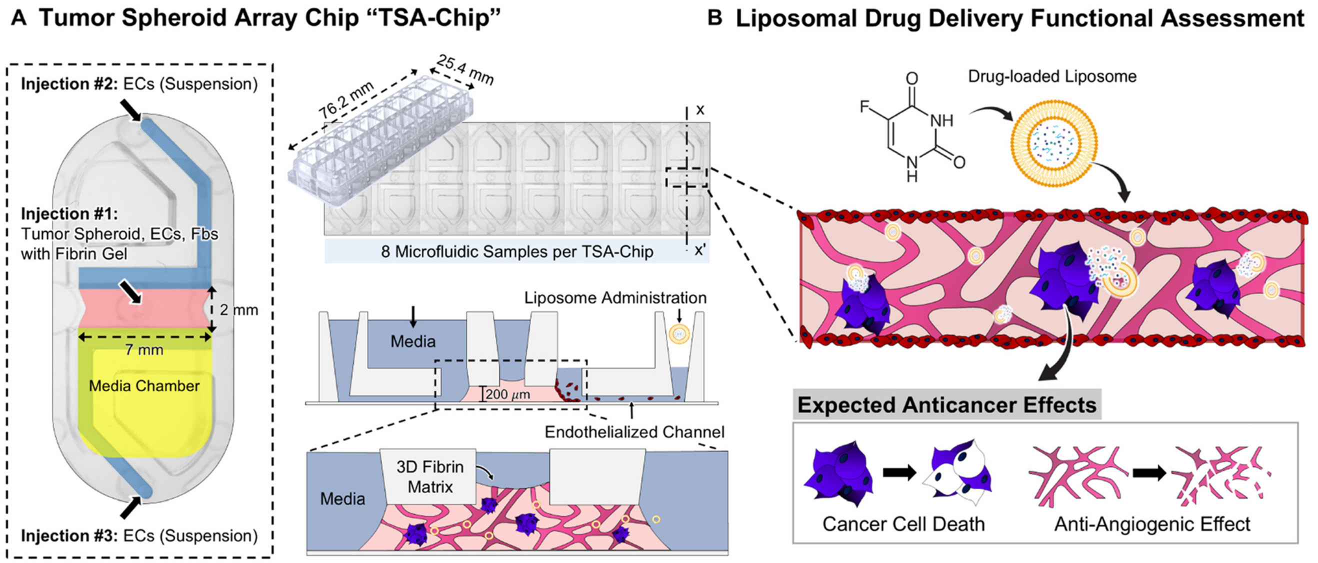

Fig. 1 Design of the TSA-Chip and mechanism of liposomal drug delivery in a perfusable TME. (A) Schematic of the TSA-Chip illustrating the sequential loading of tumor spheroids, fibroblasts (Fbs), and endothelial cells (ECs) into a fibrin matrix to construct a perfusable 3D TME. The chip supports eight independent microfluidic samples per unit and allows for drug administration through endothelialized channels. (B) Conceptual diagram of liposomal 5-FU delivery through the tumor-associated vasculature. Liposomes accumulate at the tumor site *via* the EPR effect, enabling localized drug release, cancer cell death, and anti-angiogenic effects.

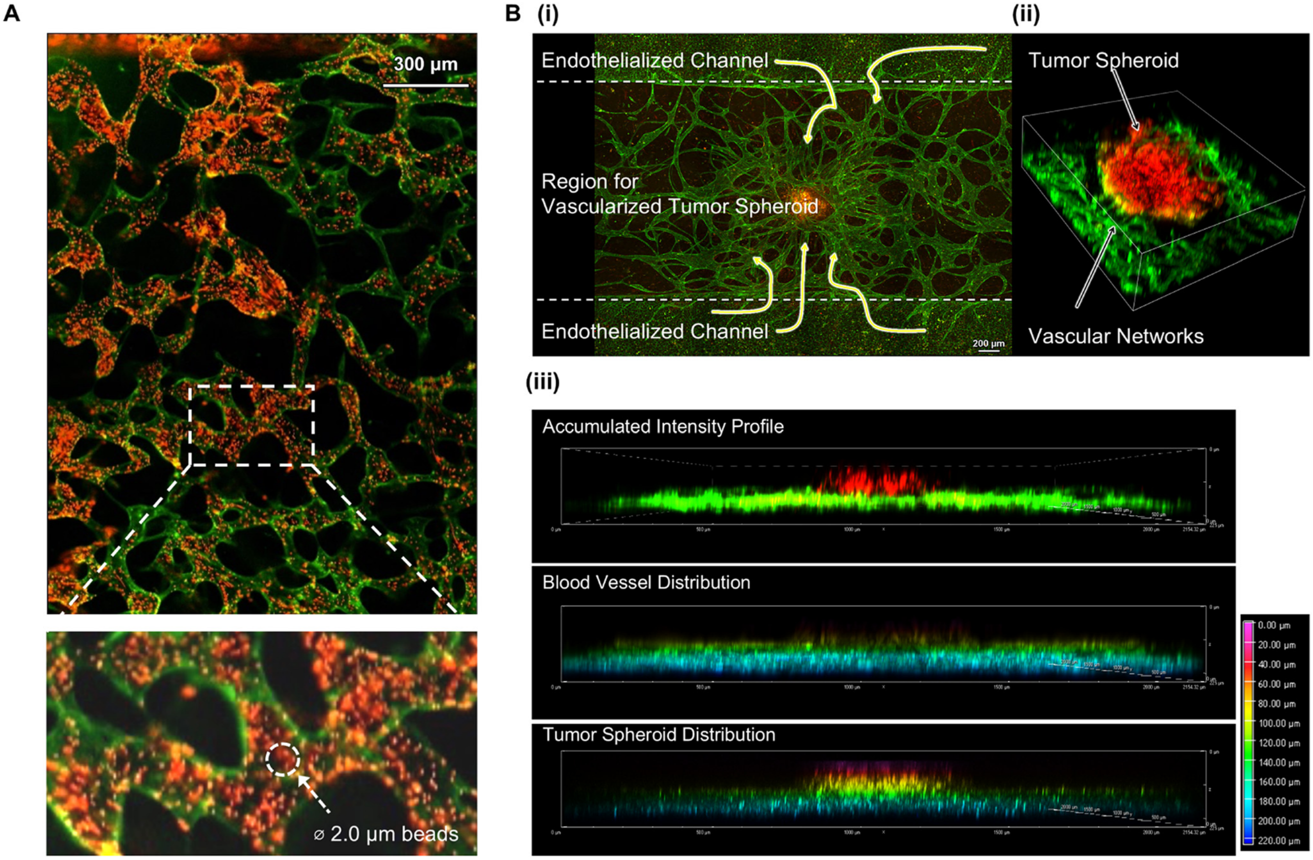

Fig. 2 Robust formation of perfusable vascular networks under optimized co-culture conditions in the TSA-Chip. (A) Fluorescence images showing perfusable vascular network. Vessels were labeled with lectin (green), and LFs were visualized with a red cell tracker. White dashed boxes indicate regions shown at higher magnification. Scale bars: 300 μm. (B-i) Confocal image of the perfusable TME at day 4, showing endothelialized side channels and a tumor spheroid (red, EpCAM) embedded in a vascularized fibrin matrix (green, lectin). Scale bar: 200 μm. (B-ii) 3D reconstruction illustrating the spatial organization of a tumor spheroid (red) within surrounding vascular networks (green). (B-iii) Depth-resolved intensity profiles showing the accumulated fluorescence signal (top), vascular distribution (middle), and tumor spheroid localization (bottom) along the *z*-axis.

Fig. 2A, increasing LF concentrations enhanced vessel formation in a dose-dependent manner. At densities ≥ 3.0 × 10^6 cells per mL, we observed denser vascular networks and increased complexity; however, excessive fibroblast proliferation at higher concentrations impaired spatial organization. An intermediate LF density of 2.0 × 10^6 cells per mL yielded the most balanced outcome—supporting robust sprouting, vessel branching, and lumen formation—without fibroblast overgrowth. This condition was therefore selected for all subsequent experiments.

Under these optimized conditions, interconnected endothelial networks formed within 4 days of culture. As shown in Fig. 2B(i), HUVECs seeded in the side channels established endothelialized interfaces that integrated with the central fibrin matrix, enabling media perfusion across the tumor compartment. Tumor spheroids became surrounded by dense microvascular networks, recapitulating the spatial arrangement of the tumor–vascular network *in vivo*. 3D reconstruction of the tumor–vessel interface revealed that CRC spheroids (EpCAM-labeled; red fluorescence) were embedded within and enveloped by vascular structures (lectin-stained; green fluorescence), forming a continuous and perfusable TME (Fig. 2B(ii)). *Z*-Stack-based intensity profiling confirmed co-localization of vascular and tumor signals throughout the matrix depth (Fig. 2B(iii)), validating that the engineered vasculature penetrated the spheroid region and provided effective transport access.

These results demonstrate that the TSA-Chip reliably supports the formation of physiologically relevant vascular networks under optimized co-culture conditions. The established architecture enables direct perfusion and sustained media exchange, providing a reproducible platform for studying drug transport, delivery efficiency, and therapeutic responses in a biomimetic TME.

3.3. Integration of multicellular tumor spheroids and characterization of 5-FU-loaded liposomes

To assess liposome-based drug delivery within a perfusable TME, we first characterized the physicochemical properties of 5-fluorouracil-loaded liposomes (5-FU-Lip) and subsequently

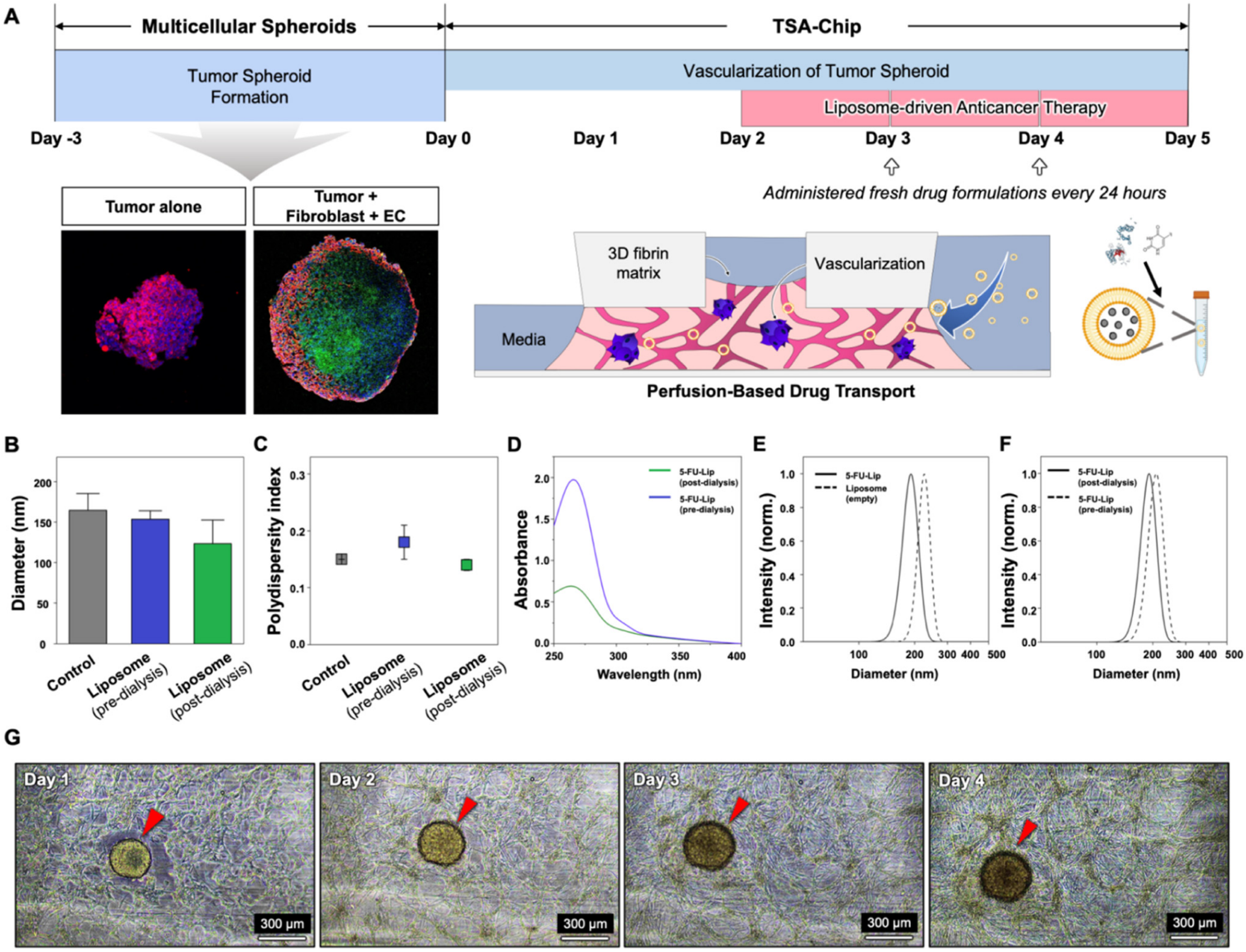

Fig. 3 Characterization of liposomal 5-FU and its application in a perfusable TSA-Chip for tumor-targeted therapy. (A) Experimental timeline illustrating the formation of multicellular tumor spheroids (day −3 to day 0), vascularization within the TSA-Chip (day 1–2), and initiation of liposomal drug administration (day 3–5). Representative confocal images show tumor spheroid without (left) or with fibroblast and endothelial cell coating (right); CD31 (green), EpCAM (red), and DAPI (blue). Liposomal 5-FU was administered daily under perfusion-based drug transport conditions. (B) Hydrodynamic diameter of liposome formulations (empty, pre-dialysis, and post-dialysis) measured by DLS. (C) Polydispersity index (PDI) of liposomes showing improved monodispersity after dialysis. (D) UV-visible spectra confirming successful 5-FU encapsulation with a characteristic absorbance peak near 266 nm. (E) Comparison of size distributions between empty liposomes and 5-FU-Lip (post-dialysis), showing no structural disruption after drug loading. (F) Size distribution of 5-FU-Lip before and after dialysis, indicating removal of unencapsulated drug without compromising nanoparticle stability. (G) Bright-field images showing stable positioning and morphology of tumor spheroids co-cultured with vasculature in the TSA-Chip over four days. Red arrowheads indicate spheroid locations. Scale bars: 300 μm.

integrated the formulation into a multicellular tumor spheroid model using the TSA-Chip platform (Fig. 3A). The liposomes were synthesized *via* the thin-film hydration method and purified by dialysis to remove the unencapsulated drug.

Dynamic light scattering (DLS) analysis revealed a reduction in average hydrodynamic diameter from 153.6 ± 10.4 nm (pre-dialysis) to 123.5 ± 29.2 nm (post-dialysis), suggesting successful removal of free 5-Fu and stabilization of liposome size distribution (Fig. 3B). The polydispersity index (PDI) decreased by 22.2% following dialysis (Fig. 3C), indicating enhanced monodispersity. UV-visible absorbance spectra confirmed 5-FU encapsulation, as evidenced by a characteristic absorption peak near 266 nm (Fig. 3D). Comparison of size distribution profiles between empty liposomes and drug-loaded formulations demonstrated no peak broadening or aggregation upon 5-FU loading (Fig. 3E). Furthermore, pre- and post-dialysis profiles of 5-FU-Lip indicated a slight reduction in particle size with preserved monodispersity, confirming that the purification process did not compromise nanoparticle integrity (Fig. 3F).[36]

The encapsulation efficiency (EE) was calculated using absorbance values at 266 nm before and after dialysis, with EE (%) = $(A_d/A_i) \times 100$, where A_i and A_d represent the total and retained 5-FU content, respectively. The resulting EE was 34.9%, which is slightly higher than values typically reported for passively loaded 5-FU (<30%), given its high aqueous solubility and low lipid bilayer affinity.[37,38] These results validate the physicochemical suitability of the liposomal formulation for use in microphysiological models.[39]

After liposome characterization, CRC multicellular spheroids were formed by co-culturing tumors with fibroblasts and endothelial cells and subsequently embedded in a 3D fibrin matrix within the TSA-Chip under hydrostatic flow conditions. Vascularization was induced over two days (days 1 and 2), and 5-FU-Lip was administered daily from day 3 to day 5 under perfusion-based delivery. Live-cell imaging confirmed that spheroids retained their structure and remained well-positioned within the chip throughout the treatment period (day 1 to day 4), supporting the feasibility of long-term vascular co-culture (Fig. 3G). The TSA-Chip, though not designed to replicate systemic pharmacokinetics, enables physiologically relevant evaluation of nanoparticle transport and localized delivery by combining vascular perfusion, interstitial flow, and dynamic drug exposure. This model facilitates functional assessment of nanomedicines, including size-dependent retention and therapeutic effects, under biomimetic flow conditions relevant to tumor-targeted therapies.

3.4. Liposomal 5-FU preserves vascular function and demonstrates EPR-like accumulation in the perfusable TSA-Chip

To evaluate tumor-selective accumulation and therapeutic effects of 5-FU–Lip, we employed the perfusable TSA-Chip that recapitulates dynamic tumor–vasculature interactions under hydrostatic flow. While the EPR effect is typically observed *in vivo* due to vascular leakage and impaired drainage, our *in vitro* model was designed to emulate its essential mechanisms through continuous perfusion, microvascular co-culture, and nanoparticle delivery. To visualize drug carrier distribution, DiI-labeled liposomes (drug-free) were administered to both 2D monolayers and TSA-Chips and tracked for 72 hours. In 2D models, liposomes rapidly diffused and accumulated uniformly across the cancer cell layer, whereas in the TSA-Chip, liposome uptake was spatially confined and temporally delayed, localizing specifically around the tumor spheroid (Fig. 4A and B). This accumulation pattern mimics the EPR effect under *in vitro* conditions.

To determine whether this behavior was tumor-specific, we compared fluorescence signals in tumor-free (tumor−) and tumor-bearing (tumor+) TSA-Chips. Only tumor+ chips exhibited appreciable peritumoral fluorescence after 48 hours (Fig. 4C), confirming that tumor presence facilitates selective liposome retention, as expected from EPR-like dynamics.

We next evaluated the cytotoxic impact of 5-FU-Lip across platforms. Three conditions—control, vehicle (empty liposomes), and 5-FU-Lip (10 μM)—were tested in 2D and 3D spheroids, and TSA-Chips using live/dead staining (Fig. 4D). Cell viability quantification revealed that 5-FU-Lip induced significant cytotoxicity in conventional models, but preserved higher viability in TSA-Chips, indicating reduced off-target toxicity under perfused conditions (Fig. 4E). Moreover, cytotoxic effects in the TSA-Chip were primarily confined to the peritumoral region.

To further explore structural remodeling, confocal imaging was conducted to visualize the vascular network surrounding tumor spheroids after treatment. Control and vehicle groups maintained dense peritumoral vasculature, while 5-FU-Lip treatment led to noticeable pruning or regression of vessels near the tumor (Fig. 4F). This structural effect was quantitatively confirmed by line intensity analysis, which revealed a marked reduction in vascular signal around spheroids only in the 5-FU-Lip group (Fig. 4G), consistent with spatially selective vascular disruption.

To functionally assess vascular integrity, we performed a FITC–dextran permeability assay (20 kDa) (Fig. 4H and I). Tumor-bearing TSA-Chips showed increased permeability compared to tumor-free controls, indicative of tumor-induced leakiness. Remarkably, 5-FU-Lip treatment restored barrier function in a dose-dependent manner. At 10 μM, permeability was reduced to levels comparable with tumor-free chips, and further decreased at 100 μM, suggesting partial normalization of the tumor-associated endothelium. Together, these results highlight the capability of the TSA-Chip to model the spatiotemporal dynamics of nanocarrier delivery and therapeutic outcomes. Liposomal 5-FU demonstrated EPR-like accumulation, peritumoral cytotoxicity, and vascular remodeling, while preserving systemic vessel function. This dual performance—localized efficacy with vascular sparing—demonstrates the translational relevance of TSA-Chip platforms in evaluating tumor-targeted nanomedicine.

3.5. Liposomal combination therapy enhances tumor suppression while preserving vascular integrity in the perfusable TSA-Chip

To assess the efficacy of single and combination anticancer drug regimens under biomimetic flow conditions, we applied both free and liposomal formulations of 5-FU, with or without the VEGFR-2 antagonist ramucirumab, in the TSA-Chip platform. Ramucirumab is a monoclonal antibody that inhibits endothelial development by blocking VEGFR-2 activation by VEGF-A, VEGF-C, and VEGF-D.[40] Because VEGFR-2 is predominantly expressed in nascent vessesls, ramucirumab selectively suppresses tumor-induced angiogenesis while sparing mature, quiescent vasculature. In contrast, 5-FU is a cytotoxic antimetabolite that disrupts DNA synthesis in proliferating tumor and endothelial cells. 5-FU-Lip prolongs circulation time and leverages the EPR effect to promote tumor-selective delivery.[41]

On day 4 of culture, drugs were perfused through the endothelialized chip channels and maintained for 72 hours. Experimental groups included: untreated control (Fig. 5A), 5-FU monotherapy (Fig. 5B), 5-FU-Lip monotherapy (Fig. 5C), combination therapy with free 5-FU and ramucirumab (Fig. 5D), and combination therapy with 5-FU-Lip and

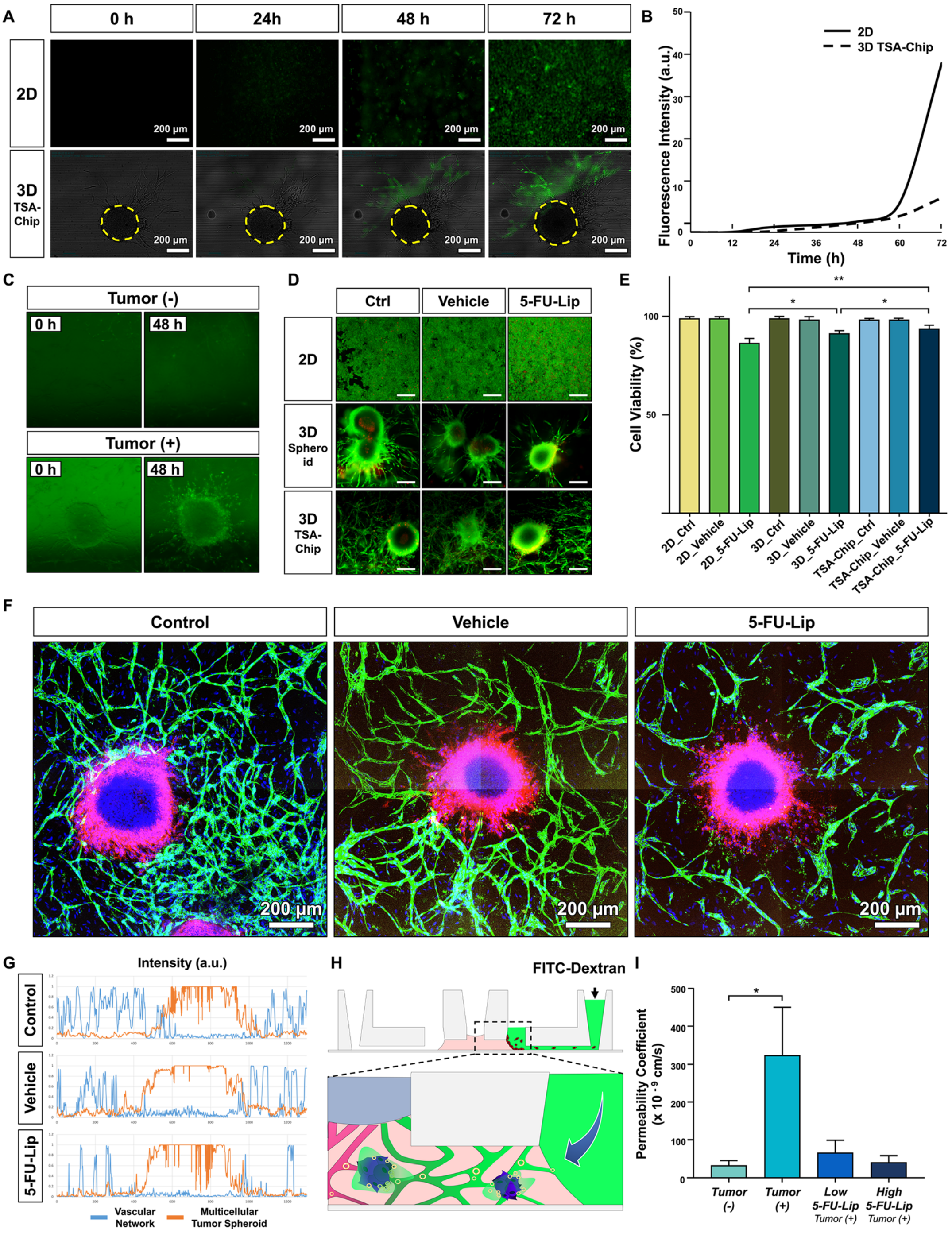

Fig. 4 Visualization of EPR-like accumulation, peritumoral cytotoxicity, and vascular remodeling induced by liposomal 5-FU in the TSA-Chip. (A) Time-lapse fluorescence imaging of DiI-labeled liposomes perfused into 2D monolayers and 3D TSA-Chips over 72 hours. Liposomes accumulated in 2D cultures, whereas spatially confined and delayed accumulation was observed around tumor spheroids in the TSA-Chip. Yellow dashed circles indicate spheroid positions. (B) Quantification of fluorescence intensity over time, demonstrating enhanced peritumoral retention in the TSA-Chip compared to uniform uptake in 2D cultures. (C) Tumor-specific liposome accumulation assessed by comparing tumor-free (tumor−) and tumor-bearing (tumor+) TSA-Chips. Accumulation was observed only in the presence of tumor spheroids after 48 hours, confirming EPR-like, tumor-selective delivery. (D) Live/dead fluorescence staining showing treatment-induced cytotoxicity in 2D and 3D spheroids, and 3D TSA-Chips under three conditions: control, vehicle (empty liposomes), and 5-FU-Lip (10 μM). Scale bars: 200 μm. (E) Quantitative analysis of cell viability across all platforms. TSA-Chip showed higher viability under 5-FU-Lip treatment compared to conventional models, indicating reduced off-target toxicity under perfusion. (F) Confocal imaging of vascular networks (green) and tumor spheroids (magenta) after 48 hours of treatment. Control and vehicle groups maintained dense peritumoral vasculature, while 5-FU-Lip treatment resulted in peritumoral vessel pruning. (G) Line intensity profiles across vascular and tumor regions extracted from panel F. A marked reduction in peritumoral vascular signal is observed in the 5-FU-Lip group, indicating spatially selective vessel remodeling. (H) Schematic illustration of the TSA-Chip perfusion setup and FITC–dextran leakage assay to evaluate barrier function. (I) Quantified permeability coefficients showing elevated leakage in tumor-bearing chips, which was significantly reduced by 5-FU-Lip treatment in a dose-dependent manner. Scale bars: 200 μm. *$p < 0.05$, **$p < 0.01$.

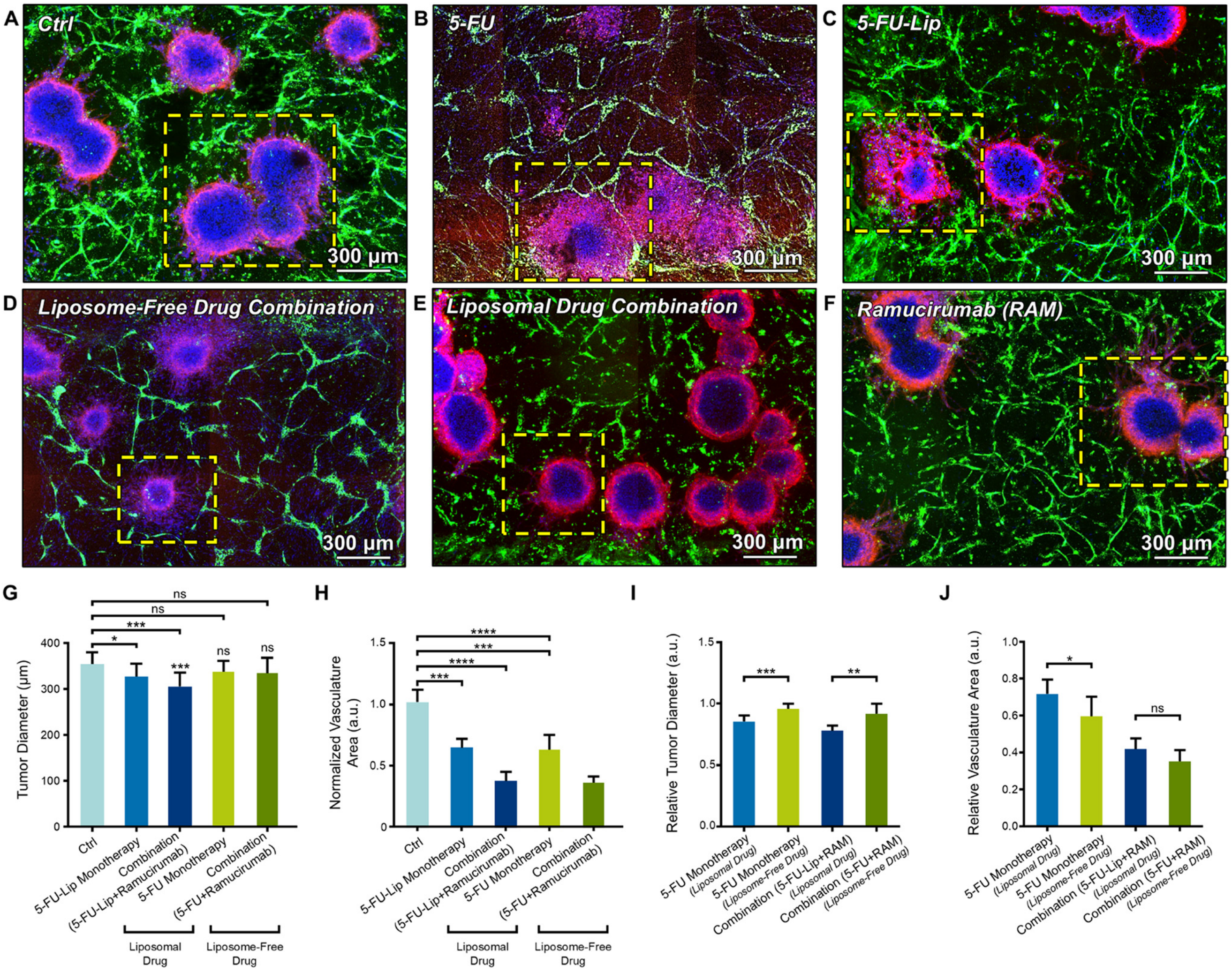

Fig. 5 Liposomal combination therapy enhances tumor suppression while preserving vascular integrity in the TSA-Chip. (A–E) Confocal fluorescence images showing tumor spheroids (magenta, EpCAM) and endothelial networks (green, lectin) after treatment in the TSA-Chip. (A) Untreated control. (B) 5-FU monotherapy (100 μM, free form). (C) 5-FU-Lip monotherapy. (D) Combination therapy with free 5-FU and ramucirumab (10 μM). (E) Combination therapy with 5-FU-Lip and ramucirumab. Yellow dashed boxes indicate representative tumor–vessel regions. Scale bars: 300 μm. (F) Ramucirumab monotherapy. (G–J) Quantitative image analysis comparing treatment responses across groups. (G) Tumor diameter. (H) Normalized vascular area. (I) Relative tumor diameter normalized to the control. (J) Relative vascular area normalized to the control. Liposomal groups include 5-FU-Lip and 5-FU-Lip + ramucirumab; liposome-free groups include 5-FU and 5-FU + ramucirumab. Data are presented as mean ± SD (n = 4 chips). Statistical analysis was performed using unpaired two-tailed t-tests. *$p < 0.05$; **$p < 0.01$; ***$p < 0.001$; ****$p < 0.0001$; ns, not significant.

ramucirumab (Fig. 5E). Tumor spheroids were visualized with EpCAM staining (magenta) and the surrounding vasculature with lectin staining (green). A schematic summary of the drug formulations and mechanisms is provided in Fig. 5F. Monotherapy with 5-FU (free form) reduced tumor spheroid size but caused some collateral vascular damage. Ramucirumab alone disrupted neovascularization while preserving the existing vasculature. In contrast, 5-FU-Lip monotherapy produced a more confined and pronounced tumor suppression effect, while maintaining surrounding vascular structure. The most substantial antitumor response was achieved with the liposomal combination therapy (5-FU-Lip + ramucirumab), which resulted in both reduced tumor diameter and suppressed angiogenic sprouting, indicating a synergistic interaction between the cytotoxic and anti-angiogenic mechanisms.

Quantitative image analysis supported these observations. Tumor diameter significantly decreased in the 5-FU-Lip monotherapy group compared to the control ($p < 0.05$), with even greater reduction in the liposomal combination group ($p < 0.001$, Fig. 5G). Vascular coverage analysis revealed a significant drop in endothelial area in the combination treatment groups, particularly with 5-FU-Lip + ramucirumab, which showed over 60% reduction compared to the control ($p < 0.0001$, Fig. 5H). In contrast, combination therapy using free 5-FU did not yield significant improvements in tumor suppression or vascular remodeling. To directly compare liposomal *versus* free drug formulations, tumor size and vascular area were normalized to untreated controls. Liposomal monotherapy consistently outperformed free 5-FU in tumor suppression ($p < 0.001$, Fig. 5I), and this advantage persisted in the combination setting ($p < 0.01$). Vascular preservation was significantly higher with 5-FU-Lip compared to its free form ($p < 0.05$, Fig. 5J), although no additional improvement was observed when combined with ramucirumab.

These results demonstrate that liposomal 5-FU enhances therapeutic efficacy while minimizing vascular damage, and that dual targeting with ramucirumab further reinforces tumor suppression.[42,43] The TSA-Chip enables spatially resolved, multiparametric analysis of drug effects on tumor and vascular compartments, supporting its utility as a preclinical screening platform for combination therapies in a perfusable tumor microenvironment.[54]

4. Discussion

Advancing nanoparticle-based therapies requires physiologically relevant *in vitro* models that recapitulate the structural and transport complexity of the TME.[53] The TSA-Chip introduced in this study integrates a perfusable microvascular network with engineered multicellular tumor spheroids to enable spatiotemporally resolved, multiparametric evaluation of nanomedicine behavior under biomimetic flow.[44] Compared to conventional spheroid-on-chip platforms,[45–47] the TSA-Chip incorporates three key innovations that enhance its utility for translational drug screening. First, the tumor spheroids are engineered through concentric co-assembly of CRC epithelial cells, fibroblasts, and endothelial cells, forming a spatially organized construct that better reflects the stromal architecture and tumor–vascular interface. This design enables biologically relevant crosstalk and a more accurate assessment of nanocarrier penetration and microenvironmental remodeling than passive aggregation approaches. Second, this study applies the platform to evaluate liposomal nanocarrier transport, accumulation, and therapeutic impact—a relatively underexplored area in dynamic TME models. Using DiI-labeled liposomes, we observed delayed but tumor-selective accumulation in the TSA-Chip, demonstrating EPR-like behavior that was absent in 2D cultures and tumor-free controls. Encapsulation of 5-FU into liposomes resulted in peritumoral cytotoxicity and vascular preservation, highlighting the ability of liposomal delivery to achieve localized therapeutic effects while maintaining systemic vessel function. Confocal imaging further revealed selective pruning of peritumoral vasculature, a process not detectable in static models. These findings emphasize the importance of vascular perfusion in modeling nanoparticle behavior and tumor–vascular interactions.[29] Third, the platform accommodates combination therapy evaluation, integrating 5-FU with ramucirumab, an anti-angiogenic agent. The combination produced synergistic effects, characterized by enhanced tumor suppression and suppression of endothelial expansion, supporting the TSA-Chip's capacity to dissect multi-drug mechanisms and optimize scheduling strategies relevant to clinical regimens.[48,49]

The perfusion offered by the TSA-Chip plays a pivotal role in recapitulating physiological transport and retention,[50,51] which static models inherently lack. Real-time imaging of fluorescent nanoparticle accumulation, tumor viability, and vascular dynamics under flow allows for high-resolution mapping of drug delivery kinetics and treatment response. This is particularly critical when evaluating agents that rely on temporal coordination, such as those inducing vascular normalization followed by cytotoxic delivery.[52] The platform's side-channel-based loading architecture enables reproducible multi-spheroid culture while maintaining spatial resolution for region-specific analysis, making it adaptable to both mechanistic studies and medium-throughput screening.

Importantly, the system distinguishes tumor-targeted cytotoxicity from off-target vascular effects, a longstanding challenge in preclinical drug evaluation. The ability to observe peritumoral drug retention, functional barrier restoration, and localized vessel remodeling enables more accurate predictions of *in vivo* performance and therapeutic index. Moreover, the differential response profiles observed across free drug, liposomal formulations, and combination therapies demonstrate the TSA-Chip's capacity for mechanism-specific efficacy deconvolution. The TSA-Chip advances the current state of microphysiological tumor models by integrating vascular perfusion, tumor architecture, and nanoparticle tracking into a single, scalable platform.[55] It supports high-content, flow-relevant analysis of nanocarrier distribution, therapeutic selectivity, and combination outcomes—positioning it as a powerful tool for precision nanomedicine development and translational oncology research.[56]

5. Conclusions

This study introduces a perfusable tumor spheroid assay chip (TSA-Chip) that enables high-content evaluation of nanocarrier-based cancer therapies within a biomimetic 3D microenvironment. By integrating engineered tumor spheroids with perfused vascular networks, the TSA-Chip supports spatially resolved, real-time analysis of nanoparticle accumulation, therapeutic response, and vascular remodeling under flow. Fluorescent liposome tracking revealed EPR-like tumor-selective accumulation, which was absent in 2D or tumor-free controls. Liposomal 5-FU treatment induced localized peritumoral cytotoxicity while preserving systemic vascular integrity, with confocal imaging and line profiling confirming vessel pruning and partial barrier normalization. Furthermore, combination treatment with ramucirumab produced synergistic tumor suppression and anti-angiogenic effects. Compared to conventional static models, the TSA-Chip advances functionality by replicating physiologic transport dynamics and enabling simultaneous monitoring of drug distribution, cytotoxicity, and vessel response. These capabilities position the TSA-Chip as a robust and scalable tool for translational oncology, facilitating precision nanomedicine screening and mechanism-driven therapeutic development.

Author contributions

Yedam Lee: conceptualization, data curation, formal analysis, investigation, methodology, project administration, validation, visualization, writing – original draft, writing – review & editing. Sujin Kim: conceptualization, data curation, formal analysis, investigation, methodology, project administration, validation, visualization, writing – original draft, writing – review & editing. Hye-Yeon Koh: data curation, formal analysis, investigation, validation, visualization, writing – original draft, writing – review & editing. Jung Y. Han: conceptualization, data curation, funding acquisition, methodology, project administration, resources, validation, visualization. Jihoon Ko: conceptualization, data curation, formal analysis, funding acquisition, methodology, project administration, resources, supervision, validation, visualization, writing – original draft, writing – review & editing.

Conflicts of interest

The authors have no conflicts of interest to declare.

Abbreviations

TME	Tumor microenvironment
TSA	Tumor spheroid array
5-FU	5-Fluorouracil
2D	Two-dimensional
3D	Three-dimensional
OoC	Organ-on-a-chip
EPR	Enhanced permeability and retention
DMPC	1,2-Dimyristoyl-*sn*-glycero-3-phosphocholine
PBS	Phosphate-buffered saline
PS	Polystyrene
CAD	Computer-aided design
UV	Ultraviolet
PSA	Pressure-sensitive adhesive
HUVEC	Human umbilical vein endothelial cells
LF	Human lung fibroblast
EGM-2	Endothelial growth medium-2
FGM-2	Fibroblast growth medium-2
DMEM	Dulbecco's modified Eagle medium
FBS	Fetal bovine serum

Data availability

Due to data confidentiality, the data supporting the findings of this study are available in a redacted form upon reasonable request.

Supplementary information (SI) is available. See DOI: https://doi.org/10.1039/d5lc00893j.

Acknowledgements

This work was supported by the National Research Foundation of Korea (NRF) through the Basic Research Program (RS-2025-24534071), funded by the Ministry of Science and ICT; the Bio Industry Technology Development Program (RS-2024-00448560) through the Ministry of Trade, Industry and Energy (MOTIE, Korea); and by the Korean ARPA-H Project (RS-2024-00512240) through the Korea Health Industry Development Institute (KHIDI), funded by the Ministry of Health and Welfare.

References

1 A. Abbott, *Nature*, 2003, **424**, 870–873.
2 J. Ko, J. Song, Y. Lee, N. Choi and H. N. Kim, *Lab Chip*, 2024, **24**, 1542–1556.
3 N. Carragher, F. Piccinini, A. Tesei, O. J. T. Jr, M. Bickle and P. Horvath, *Nat. Rev. Drug Discovery*, 2018, **17**, 606–606.
4 S. Y. Park, H. J. Hong and H. J. Lee, *BioChip J.*, 2023, **17**, 24–43.
5 G. Rossi, A. Manfrin and M. P. Lutolf, *Nat. Rev. Genet.*, 2018, **19**, 671–687.
6 S. Yoo and H. J. Lee, *Cells Tissues Organs*, 2025, **214**, 128–147.
7 C. M. Leung, P. De Haan, K. Ronaldson-Bouchard, G.-A. Kim, J. Ko, H. S. Rho, Z. Chen, P. Habibovic, N. L. Jeon and S. Takayama, *Nat. Rev. Methods Primers*, 2022, **2**, 33.
8 J. Ko, S. Hyung, Y. J. Heo, S. Jung, S. T. Kim, S. H. Park, J. Y. Hong, S. H. Lim, K.-M. Kim and S. Yoo, *Biomaterials*, 2024, **306**, 122504.
9 Y. Nashimoto, T. Hayashi, I. Kunita, A. Nakamasu, Y.-s. Torisawa, M. Nakayama, H. Takigawa-Imamura, H. Kotera, K. Nishiyama, T. Miura and R. Yokokawa, *Integr. Biol.*, 2017, **9**, 506–518.
10 C. Quintard, E. Tubbs, G. Jonsson, J. Jiao, J. Wang, N. Werschler, C. Laporte, A. Pitaval, T.-S. Bah and G. Pomeranz, *Nat. Commun.*, 2024, **15**, 1452.
11 S. Zhang, Z. Wan and R. D. Kamm, *Lab Chip*, 2021, **21**, 473–488.
12 A. Sobrino, D. T. T. Phan, R. Datta, X. Wang, S. J. Hachey, M. Romero-López, E. Gratton, A. P. Lee, S. C. George and C. C. W. Hughes, *Sci. Rep.*, 2016, **6**, 31589.
13 C. Bayona, L. Alza, T. Ranđelović, M. C. Sallán, A. Visa, C. Cantí, I. Ochoa, S. Oliván and J. Herreros, *Cell Death Dis.*, 2024, **15**, 127.
14 S. Lee, H. Kim, B. S. Kim, S. Chae, S. Jung, J. S. Lee, J. Yu, K. Son, M. Chung and J. K. Kim, *Nat. Commun.*, 2024, **15**, 230.
15 M. R. Haque, C. R. Wessel, D. D. Leary, C. Wang, A. Bhushan and F. Bishehsari, *Microsyst. Nanoeng.*, 2022, **8**, 36.
16 K. Haase, G. S. Offeddu, M. R. Gillrie and R. D. Kamm, *Adv. Funct. Mater.*, 2020, **30**, 2002444.
17 G. Visani, F. Loscocco and A. Isidori, *Nanomedicine*, 2014, **9**, 2415–2428.

18 X. Chen, Y. S. Zhang, X. Zhang and C. Liu, *Bioact. Mater.*, 2021, **6**, 1012–1027.

19 M. V. Braham, A. K. Deshantri, M. C. Minnema, F. C. Öner, R. M. Schiffelers, M. H. Fens and J. Alblas, *Int. J. Nanomed.*, 2018, 8105–8118.

20 A. Ghahremanloo, B. Erfani, F. Asgharzadeh, S. Mansoori, F. Gheybi and S. I. Hashemy, *Sci. Rep.*, 2025, **15**, 9798.

21 J. Y. Han, J. N. La Fiandra and D. L. DeVoe, *Nat. Commun.*, 2022, **13**, 6997.

22 M.-A. Jourdain and J. Eyer, *J. Controlled Release*, 2024, **376**, 732–752.

23 G. Wang, B. Wu, Q. Li, S. Chen, X. Jin, Y. Liu, Z. Zhou, Y. Shen and P. Huang, *Small*, 2020, **16**, 2004172.

24 E. Lopez-Vince, C. Wilhelm and T. Simon-Yarza, *Drug Delivery Transl. Res.*, 2024, **14**, 2216–2241.

25 Y. Lee, J. Min, S. Kim, W. Park, J. Ko and N. L. Jeon, *Adv. Healthcare Mater.*, 2025, **14**, 2401927.

26 Z. Wan, M. A. Floryan, M. F. Coughlin, S. Zhang, A. X. Zhong, S. E. Shelton, X. Wang, C. Xu, D. A. Barbie and R. D. Kamm, *Adv. Healthcare Mater.*, 2023, **12**, 2201784.

27 W. Wang, P. Joyce, K. Bremmell, R. Milne and C. A. Prestidge, *Pharmaceutics*, 2022, **14**, 221.

28 O. Udofot, K. Affram, T. Smith, B. Tshabe, S. Krishnan, M. Sachdeva and E. Agyare, *J. Nat. Sci.*, 2016, **2**, e171.

29 J. Fang, W. Islam and H. Maeda, *Adv. Drug Delivery Rev.*, 2020, **157**, 142–160.

30 D. Peer, J. M. Karp, S. Hong, O. C. Farokhzad, R. Margalit and R. Langer, *Nano-Enabled Med. Appl.*, 2020, 61–91.

31 K. Gokita, J. Inoue, H. Ishihara, K. Kojima and J. Inazawa, *Mol. Ther.–Nucleic Acids*, 2020, **19**, 330–338.

32 D. Liu, F. Yang, F. Xiong and N. Gu, *Theranostics*, 2016, **6**, 1306–1323.

33 A. M. Thomas, A. I. Kapanen, J. I. Hare, E. Ramsay, K. Edwards, G. Karlsson and M. B. Bally, *J. Controlled Release*, 2011, **150**, 212–219.

34 J. Ko, D. Park, J. Lee, S. Jung, K. Baek, K. E. Sung, J. Lee and N. L. Jeon, *Nat. Rev. Bioeng.*, 2024, **2**, 453–469.

35 H. Lee, S. Kim, M. Chung, J. H. Kim and N. L. Jeon, *Microvasc. Res.*, 2014, **91**, 90–98.

36 Y. Tang, F. Soroush, J. B. Sheffield, B. Wang, B. Prabhakarpandian and M. F. Kiani, *Sci. Rep.*, 2017, **7**, 9359.

37 M. Glavas-Dodov, E. Fredro-Kumbaradzi, K. Goracinova, M. Simonoska, S. Calis, S. Trajkovic-Jolevska and A. A. Hincal, *Int. J. Pharm.*, 2005, **291**, 79–86.

38 J. O. Eloy, M. Claro de Souza, R. Petrilli, J. P. A. Barcellos, R. J. Lee and J. M. Marchetti, *Colloids Surf., B*, 2014, **123**, 345–363.

39 R. Huang, H. Song, S. Li and X. Guan, *Food Chem.: X*, 2025, **25**, 102149.

40 C. S. Fuchs, J. Tomasek, C. J. Yong, F. Dumitru, R. Passalacqua, C. Goswami, H. Safran, L. V. Dos Santos, G. Aprile and D. R. Ferry, *Lancet*, 2014, **383**, 31–39.

41 D. B. Longley, D. P. Harkin and P. G. Johnston, *Nat. Rev. Cancer*, 2003, **3**, 330–338.

42 L. Bomgaars, J. Geyer, J. Franklin, G. Dahl, J. Park, N. Winick, R. Klenke, S. Berg and S. Blaney, *J. Clin. Oncol.*, 2004, **22**, 3916–3921.

43 H. Nsairat, D. Khater, U. Sayed, F. Odeh, A. Al Bawab and W. Alshaer, *Heliyon*, 2022, **8**, e09394.

44 J. Ahn, D.-H. Kim, D.-J. Koo, J. Lim, T.-E. Park, J. Lee, J. Ko, S. Kim, M. Kim, K.-S. Kang, D.-H. Min, S.-Y. Kim, Y. Kim and N. L. Jeon, *Acta Biomater.*, 2023, **165**, 153–167.

45 J. Ko, J. Ahn, S. Kim, Y. Lee, J. Lee, D. Park and N. L. Jeon, *Lab Chip*, 2019, **19**, 2822–2833.

46 N. Shin, Y. Kim, J. Ko, S. W. Choi, S. Hyung, S.-E. Lee, S. Park, J. Song, N. L. Jeon and K.-S. Kang, *Biotechnol. Bioeng.*, 2022, **119**, 566–574.

47 J. Song, J. Ko, N. Choi, N. L. Jeon and H. N. Kim, *Organoid*, 2023, **3**, e6.

48 E. B. Garon, T.-E. Ciuleanu, O. Arrieta, K. Prabhash, K. N. Syrigos, T. Goksel, K. Park, V. Gorbunova, R. D. Kowalyszyn, J. Pikiel, G. Czyzewicz, S. V. Orlov, C. R. Lewanski, M. Thomas, P. Bidoli, S. Dakhil, S. Gans, J.-H. Kim, A. Grigorescu, N. Karaseva, M. Reck, F. Cappuzzo, E. Alexandris, A. Sashegyi, S. Yurasov and M. Pérol, *Lancet*, 2014, **384**, 665–673.

49 S. Lorenzen, A. Schwarz, C. Pauligk, E. Goekkurt, G. Stocker, J. R. Knorrenschild, G. Illerhaus, T. Dechow, M. Moehler, J.-C. Moulin, D. Pink, M. Stahl, M. Schaaf, T. O. Goetze and S.-E. Al-Batran, *BMC Cancer*, 2023, **23**, 561.

50 M. R. Dreher, W. Liu, C. R. Michelich, M. W. Dewhirst, F. Yuan and A. Chilkoti, *J. Natl. Cancer Inst.*, 2006, **98**, 335–344.

51 M. W. Dewhirst and T. W. Secomb, *Nat. Rev. Cancer*, 2017, **17**, 738–750.

52 R. K. Jain, *Science*, 2005, **307**, 58–62.

53 J. Ahn, D.-H. Kim, D.-J. Koo, J. Lim, T.-E. Park, J. Lee, J. Ko, S. Kim, M. Kim and K.-S. Kang, *Acta Biomater.*, 2023, **165**, 153–167.

54 S. Jung, S. Cheong, Y. Lee, J. Lee, J. Lee, M.-S. Kwon, Y. S. Oh, T. Kim, S. Ha and S. J. Kim, *ACS Nano*, 2024, **18**, 24909–24928.

55 B. Zhang, A. Korolj, B. F. L. Lai and M. Radisic, *Nat. Rev. Mater.*, 2018, **3**, 257–278.

56 D. Liu, F. Yang, F. Xiong and N. Gu, *Theranostics*, 2016, **6**, 1306.